Critical Barriers to Successful Implementation of Earth-Abundant, Mn-Rich Cathodes for Vehicle Applications and Beyond: The Effect of Particle Morphology

Arturo Gutierrez,[1] Joel T. Kirner,[1,*] Mahmoud Tamadoni Saray,[2] Maxim Avdeev,[3,4] Linxiao Geng,[5] Reza Shahbazian Yassar,[2] Wenquan Lu,[1] and Jason Croy[1]

[1]Chemical Sciences and Engineering Division, Argonne National Laboratory, Lemont, Illinois 60439, United States of America
[2]Department of Mechanical and Industrial Engineering, University of Illinois at Chicago, Chicago, Illinois 60607, United States of America
[3]Australian Centre for Neutron Scattering, Australian Nuclear Science and Technology Organisation, Lucas Heights, New South Wales 2234, Australia
[4]School of Chemistry, The University of Sydney, Sydney, New South Wales 2006, Australia
[5]Energy and Transportation Science Division, Oak Ridge National Laboratory, Oak Ridge, Tennessee 37996, United States of America
[*]Electrochemical Society Member

Abstract

As the search for improved and next-generation cathodes continues, it is clear that a deeper understanding of synthesis–structure–electrochemical property relationships is of critical importance. The effects of primary and secondary particle morphologies on various transition metal oxides have been studied, but new findings are still being reported. To date, few studies have focused on the effects of particle morphologies on Li-and Mn-rich oxides (>50% Mn) and even fewer studies have focused on the influence over key properties such as electrode-level impedance. Herein we report the effects of particle morphologies on the area-specific-impedance (ASI) and thermal behavior of Li- and Mn-rich oxides. Samples with a fixed, layered–layered–spinel (LLS), composition were synthesized with differing primary morphologies and tested under standardized, full-cell protocols. The results suggest that smaller primary particle size (i.e., higher surface area) leads to lower overall ASI, a delay in the increasing impedance at low states-of-charge (SOCs), and surprisingly, improved thermal behavior.

Nothing in recent times epitomizes the push towards fully electrifying the transportation sector quite like the development of the all-electric Ford F-150. Being the most popular vehicle in the U.S., the F-150 represents true market demand, and the all-electric version is a seemingly critical turning point in the quest for electrification. This paradigm shift is a reminder that the development of a more diverse portfolio of battery materials will be key in sustaining electric vehicle (EV) markets with respect to raw materials, supply chains, and cost. In particular, metal-oxide cathodes based on earth-abundant elements could play a critical role in supporting sustainable market growth. Lithium- and manganese-rich nickel-manganese-cobalt (LMR-NMC) oxides are among the few classes of cathode materials based largely on earth abundant elements (i.e., Mn) that also offer inherently large specific energies. These oxides are currently being pursued as viable options, notwithstanding several principal challenges.[1,2]

Among these challenges is a high area-specific impedance (ASI, $\Omega \cdot cm^2$) at low states of charge (LSOC), denoted hereafter as Ω_{LSOC}. Though the literature for this topic is relatively scarce, some hypotheses as to the underlying causes of Ω_{LSOC} have been proposed. For instance, Teufl et al. suggested the impedance issue in LMR-NMC stems from a disordered surface phase that forms as a result of oxygen loss during activation.[3,4] On the other hand, research at Argonne shows that the bulk plays a significant role in Ω_{LSOC} through changes in local structures linked to Li/Mn ordering (e.g., $LiMn_6$) and electrochemical activation thereof.[5,6] The most salient effect of Ω_{LSOC} is that under high-rate conditions, a significant percentage of the discharge capacity can be inaccessible, as lithium diffusion through the disordered domains is substandard. Though Ω_{LSOC} in LMR-NMCs can be directly correlated to the changes that take place on a local level, it is also evident from the literature that macroscopic considerations, such as particle morphology, can also play a significant role in electrode-level properties such as impedance and rate.[7–9] Therefore, it is also of interest to understand how different morphologies might affect Ω_{LSOC} in LMR-NMCs and to what extent morphology might be used to improve important properties such as ASI.

Currently, most commercially available metal-oxide cathode powders have ~spherical secondary particle morphologies (D50: ~10–15 microns) which are, in turn, made up of smaller primary particles (10s–100 s of nanometers), where the secondary structures have varying levels of porosity. The importance of the primary particle size and the secondary particle porosity to the electrochemical performance of LMR-NMC oxides has been noted previously,[10–13] yet only one such investigation, conducted by Mao et al., directly studied Ω_{LSOC} with respect to morphology.[14] However, the purpose of that work was to investigate the root cause of Ω_{LSOC} (i.e., surface vs bulk), where it was concluded that both the bulk and surface contributed comparably at low SOCs, somewhat in contrast to the works mentioned above.[3–6]

Particle morphologies can also influence other key characteristics such as safety/thermal stability and much work has been done in this area, particularly for layered transition metal oxides (e.g., NMCs). Studies have focused on different aspects that contribute to the thermal stability such as compositional differences,[15–18] SOCs,[19] and interactions with the electrolyte.[20,21] Some work investigating the thermal stability of LMR-NMCs also exists.

For example, the thermal stability of particular LMR-NMCs have been compared to other chemistries and were found to exhibit higher decomposition onset temperatures compared to $LiCoO_2$[22] and single crystal NMC-811,[23] while displaying lower thermal stabilities when compared to NMC-111.[24] Furthermore, the various phase transitions that occur in a delithiated LMR-NMC, in the presence or absence of electrolyte, have also been investigated.[25] To our knowledge, however, there have been no studies investigating the effects of particle morphologies (surface area/particle size) on the thermal stability of LMR-NMCs.

Herein we present results on a series of LMR-NMC cathode-oxides containing a small, integrated spinel component, denoted as layered–layered–spinel (LLS), and described in detail elsewhere.[26–28] LLS particles were synthesized under conditions that gave similar compositions and secondary particle sizes, but which had different primary particle sizes. These oxides are used to directly probe differences in Ω_{LSOC}, as well as their relative thermal stabilities, as measured by differential scanning calorimetry (DSC). Results are discussed in terms of primary particle size, secondary porosity, and surface area.

Experimental

Synthesis of layered–layered–spinel oxides.—LLS cathode powders were synthesized using $Mn_{0.53}Ni_{0.28}Co_{0.19}CO_3$ carbonate precursors prepared in a continuously stirred tank reactor. A 4 L tank was filled with an initial volume of 3 L of distilled water with 0.05 M of ammonium hydroxide. The tank reactor was sealed and N2 was flowed through the tank to avoid oxidation of the product. The stirring speed, temperature, and pH were controlled at 1000 RPM, 35°C, and 8.3, respectively, for the remainder of the reaction. Solutions of 2 M NMC sulfates (w/ appropriate NMC ratios), 2 M sodium carbonate (Na_2CO_3 for pH control), and 0.05 M ammonium hydroxide (NH_4OH) were pumped into the reactor, allowing for a 6-h residence time. The product was collected after four residence times (24 h), then washed and dried under flowing N_2 gas at 130 °C.

The dried transition metal carbonate was then mixed with lithium carbonate (Li2CO3) to obtain a target composition containing between 5%–10% spinel and fired at 900 °C for 20 h in air, followed by natural cooling in the furnace.

X-ray diffraction.—High-energy synchrotron x-ray powder diffraction (HE-XRD) data were collected using beamline 11-ID-C at the Advanced Photon Source, Argonne National Laboratory, using an average wavelength of 0.1173 Å.

Neutron powder diffraction (NPD).—The powder samples were loaded into 6 mm diameter cylindrical vanadium cans and NPD data were collected on the high-resolution powder diffractometer Echidna[29] at the Australian Centre for Neutron Scattering, using neutrons with a wavelength of 1.6215 Å. Rietveld analysis of the NPD data was performed using the GSAS code with EXPGUI frontend.[30,31]

Transmission electron microscopy (TEM).—A probe spherical aberration corrected JEOL TEM/STEM ARM 200CF equipped with a cold field emission gun at 200 kV was used for

detailed microstructural characterization. The cathode samples were scratched from the current collector and drop cast on a holey carbon supported Cu TEM grid. Scanning transmission electron microscopy (STEM) images were collected using HAADF, LAADF detectors with 90, 40 and 23 mrad detector collection angles, respectively. The electron beam has a convergence angle of 17.8 mrad. DigitalMicrograph software (Gatan Inc.) was utilized for all STEM image processing.

Scanning electron microscopy.—Images of the particle morphologies were investigated using a Hitachi S-4700-II microscope in the Electron Microscopy Center, Argonne National Laboratory.

Electrochemical characterization.—A slurry of the baseline LLS, polyvinylidene fluoride (PVDF), and C45 carbon (84, 8, 8 wt%, respectively) in NMP solvent was prepared by Thinky mixer and cast on aluminum foil to prepare electrodes. Graphite (~92%—calendered porosity of ~38%) mixed with conductive carbon and PVDF binder was used as the anode in full-cells, or lithium metal (300 μm thickness) was used as the anode in half-cells. All electrodes were dried in a vacuum oven overnight before cells were assembled in an argon-filled glovebox where the moisture and oxygen contents are controlled near or below 1 ppm. The full-cell N:P ratio was kept between 1.1 and 1.15 to ensure the capacity was always cathode-limited. On average, the loading of the cathodes used for full-cells was ~9 mg cm^{-2} (60 μm thick—no foil) with an estimated porosity of ~40%. The loading on electrodes used for half-cell testing was ~5 mg cm^{-2} (40 μm thick—no foil) with an estimated porosity of ~40%. A Celgard 2325 separator was used in all cells. The electrolyte (Gen2) was 1.2 M $LiPF_6$ in ethylene carbonate: ethyl methyl carbonate (EC:EMC, 3:7 by weight).

All cycling was carried out with 2032-type coin-cells in temperature controlled (30 °C) chambers. Details about testing vs lithium metal are provided in the body of the article. Details about the cycling protocol used for testing against graphite anodes can be found in Ref. 32. Briefly, the protocol consists of the following elements:

- A formation cycle, which allows for the wetting of electrodes and formation of the solid-electrolyte interphase on graphite. This formation cycle is only done once at the beginning of each test protocol. The first cycle includes an activation between 4.6 and V (vs graphite) at C/10. All following cycles are carried out between 4.4 and 2.5 V.

- Hybrid-pulse-power-characterization (HPPC) preparation
cycles, for three purposes:

  i. To inspect the voltage profile under low current (C/10) during discharge to reduce the effects of impedance.

  ii. To probe the effect of a high current (1 C) on the capacity during discharge (one cycle).

  iii. To gather information about the impedance as a function of the SOC of the cell.

- Aging cycles, used to accelerate the degradation of the cells by using a 3-h hold at the top of charge (4.4 V). These cycles are carried out using a current that allows a full discharge in 3 h (C/3).

Thermal analysis.—LLS half-cells with Li metal anodes under-went 1 activation cycle (4.6–2.0 V), followed by 3 formation cycles (4.5–2.5 V) at a C/10 rate (~0.2 mA g^{-1} active material). The chemical composition obtained via inductively coupled plasma–optical emission spectroscopy (ICP-OES) of the pristine material ($Li_{1.18}Mn_{0.53}Ni_{0.28}Co_{0.19}O_y$) was used to calculate the theoretical capacity for extraction of all Li^+ (311 mAh $g)^{-1}$. This value and the cumulative irreversible capacity loss during formation cycles were used to calculate the charge capacity needed to charge each cell to reach approx. $Li_{0.3}MO_y$ end state for thermal testing. Alternatively, formed cells were galvanostatically charged (C/10) to 4.5 V, then potentiostatically held for 4 h.

Coin cells were disassembled in an argon-filled glove box, carefully collecting the cathode with non-conductive tweezers to avoid short-circuits. Harvested cathodes were soak-rinsed (gentle swirling) twice for 60 s in 1 ml of EMC solvent to remove residual electrolyte, then dried for 10 min under dynamic vacuum in the glovebox antechamber. Cathode laminate powders were scraped from each dried cathode using a size 2 A tweezer, and the recovered powder was carefully weighed (2–3 mg) into a DSC capsule (reusable stainless-steel high-pressure capsules, 30 μl volume, Perkin Elmer). Just before measurement, Gen2 electrolyte was added to each capsule by auto pipette with a ratio of 1 μl electrolyte per 1 mg of cathode powder. Each capsule was hermetically sealed with a gold-plated copper pressure seal and screw cap and tightened with the supplied torque clutch sealing tool. Capsules were then removed from the glove box and loaded into the DSC instrument (Perkin Elmer DSC 6000), where they were tested versus an empty reference capsule also sealed under argon. DSC measurements were recorded between 30 °C–400 °C using a ramp rate of 10 °C min^{-1}. At least two samples were taken from each cell. Before use, reusable DSC capsules were cleaned of soot using a Dremel tool, followed by 10 min of sonication in water, then ethanol, rinsed with distilled water, then dried overnight at 75 °C under dynamic vacuum.

Results and Discussion

Characterization of powder samples.—The samples of interest for this work were prepared by taking the baseline powder, fired at 900 °C, and splitting it into four different batches, then refiring each of the smaller batches for 10 h at one of four target temperatures: 925, 950, 975, or 1000 °C. This two-step process was adopted to minimize compositional differences in the lithium-to-transition metal (Li/TM) ratios caused by Li evaporation. Chemical analysis via ICP confirmed the samples experienced no lithium loss because of the different firing temperatures (each showed $Li_{1.18}Mn_{0.53}Ni_{0.28}Co_{0.19}O_y$), consistent with the target spinel composition of ~6%. The samples are referred to as LLS_925 °C, LLS_950 °C, LLS_975 °C, and LLS_1000 °C from here forward. HE-XRD revealed good crystallinity for each powder (Fig. 1) where the main peaks can be indexed to R-*3m*, excluding the ordering peaks near 1.57° 2θ that are associated with the C2/*m*

space group. Although the samples revealed no differences in terms of crystal phase, there were noticeable differences in the broadening of the peaks as shown for the (003) peaks in the inset of Fig. 1. The peaks' full width at half maximum (FWHM) from each sample was found to decrease as the firing temperature increased (see table in Fig. 1). Several factors can contribute to the changing FWHM, including strain and crystallite size. The peak width is inversely proportional to crystallite size according to the Scherrer equation. Therefore, the crystallite size may be expected to grow across the sample set as a function of increasing firing temperature. The particle morphology for each of the samples is shown in the SEM images of Fig. 2. The secondary particle size did not change as the firing temperature increased and the overall size distribution for each sample was similar. The median diameter of secondary particles (D_{50}) was corroborated by particle size analysis to be ~19 μm for all samples. On the other hand, the primary particle size steadily increased as the firing temperature increased (see inset images of Fig. 2). On visual inspection of primary particles, it is estimated the sizes are 100, 200, 400, and 800 nm for LLS_925 °C LLS_950 °C, LLS_975 °C, and LLS_1000 °C, respectively. An analysis on the FWHM of the samples (see supplementary data (available online at stacks.iop.org/JES/169/020574/mmedia) determined that strain contributions to the peak broadening increased with firing temperature, suggesting that if the strain were playing a major role in the observed FWHM, the peak broadening would have occurred as firing temperature *increased*. Therefore, it is concluded that the changing primary particle size is the major contributor to the peak broadening observed in the HE-XRD data.

Because the intent of this work was to study differences in impedance (i.e., barriers to Li diffusion) caused by morphological differences, it is critical to determine what, if any, measurable structural differences might be present between the samples of interest. Therefore, neutron powder diffraction was carried out on the samples of interest and structural parameters along with the amount of Li/Ni mixing was determined via Rietveld analysis (see supplementary data for details). Notably, it was determined that the difference (Fig. 1b) in Li/Ni mixing between the samples was ~0.5% (within the error), suggesting differences in barriers to lithium diffusion cannot be reasonably attributed to differences in Li/Ni mixing between the samples.

The BET specific surface area of each sample was measured and found to decrease as the firing temperature increased: 3.8 $m^2\ g^{-1}$, 2.8 $m^2\ g^{-1}$, 1.3 $m^2\ g^{-1}$, and 1.0 $m^2\ g^{-1}$ for 925, 950, 975, and 1000 °C, respectively. A cross-section image of a representative particle from each powder is shown in figure S6, which shows how the internal porosity changed as a function of firing temperature. The initial characterization of the powders shown above revealed a clear difference between the samples with respect to surface area and primary particle size, while the composition and long-range order (via ICP, XRD and NPD) of the samples remained unchanged. Shorter range probes, including Raman and nuclear magnetic resonance (NMR) spectroscopies, also revealed no quantifiable differences (not shown) between the samples.

Electrochemical testing vs $Li^{\pm}$.—Each of the samples was tested in coin-type half-cells (vs $Li^{+/0}$) using a protocol designed to gather useful electrochemical information quickly (~10 cycles) as described in Ref. 33. The results are summarized in Fig. 3. Each sample was

charged up to 4.6 V during activation (see Fig. 3a) and, except for small differences near 3.75 V, the profiles overlap for much of the charging process. Additionally, the samples delivered comparable capacities at the top of charge (265, 262, 261, and 257 mAh/g for 925, 950, 975, and 1000 °C, respectively), signifying the samples have undergone a similar level of activation and utilization of Li. The voltage profiles also overlapped during the 1st cycle discharge until the voltage reached ~3.6 V, at which point some deviation occurred and a systematic decrease in capacity and first-cycle efficiency (FCE) was delivered by samples with increasing firing temperature (232, 225, 216, and 209 mAh/g for 925, 950,975, and 1000 °C, respectively). The extra discharge capacity from lower-T samples is delivered near ~3.5 V, as can be seen from the 1st cycle dQ/dV shown in Fig. 3c. During subsequent cycles, the samples prepared at lower temperatures continued to deliver higher charge and discharge capacity (10th cycle voltage profiles are compared in Fig. 3b), and this extra redox activity occurs at potentials <3.5 V (Fig. 3d).

Additional experiments showed that if a low voltage hold was carried out at bottom of discharge, then differences in 1st cycle discharge capacities between all samples could be minimized (<10 mAh/g). Furthermore, high temperature cycling (55 °C) of LLS_1000 °C showed similar first-cycle capacities and profiles as the LLS_925 °C (Figure S7), including the ~3.75 V charge peak mentioned above, as well as similar redox activity < 3.5 V. These data reveal that the observed differences in electrochemical performance between the cathode samples are mostly kinetic in nature, suggesting that the energy barrier for the insertion of Li^+ into the post-activation sites created below ~3.5 V increases as the primary particle sizes increase (increasing firing temperature). The redox activity in this voltage range has been associated with various types of electrochemical mechanisms such as transition metal migration[34] and oxygen activity.[35] In reality, these two mechanisms are correlated in LMR-NMC cathodes and can occur simultaneously during cycling.[36,37]

Adding to the complexity of these mechanisms are considerations concerning surface versus bulk contributions. Previous studies have shown that layered–layered LMR cathodes reorganize to disordered spinel-like phase preferentially on the surface during initial activation, which may then propagate into the particle bulk. Furthermore, the magnitude of oxygen loss and surface reconstruction, especially for unprotected particles, have been reported to influence the sites that develop at low voltages during the first-cycle activation.[3,4] Given that the samples in the present study are initially compositionally and structurally indistinguishable (i.e., same intended excess Li and Mn contents with similar local and long-range crystal ordering), the systematic differences in the electrochemical signatures in the region < 3.5 V are likely attributable to the differences in surface areas and/or primary particle sizes by way of their response to the activation process. Indeed, the kinetic nature of the differences shown in Fig. 3, particularly on the discharge process, may suggest limited oxygen diffusion/release from the larger primary particles (LLS_1000 °C) relative to the much smaller primaries of LLS_925 °C, thereby altering the lithium insertion on discharge. Preliminary gassing studies do indeed show more gas evolution, in the form of CO_2, from the LLS_925 °C compared to the LLS_1000 °C (Figure S8). The challenges of quantifying oxygen loss from these materials are well-known and is an ongoing topic of study and debate.[38–40] However, the preliminary results are not at odds with the hypothesis of kinetically hindered oxygen release from larger primary particles. An ongoing

investigation of the gassing differences is underway and will be reported in the future.

Despite the differences in gassing exhibited by LLS_925 °C and LLS_1000 °C, TEM analysis of the surfaces revealed similar reconstruction after the initial 4 activation cycles (see Fig. 4). In general, both samples contained a 2–3 nm surface reconstruction layer that consisted of a transition from layered structure (R-*3m*) in the bulk to rocksalt (*Fm-3m*) on the outer surface, with an intergrown layer of spinel (*Fd-3m*) in between. A representative example of what was observed on the surface of LLS_925 °C (Fig. 4a) and LLS_1000 °C (Fig. 4b) shows the similarities between the surface structures on both samples. Further characterization of each of the samples is provided in supplementary data.

Beginning of life (BOL) impedance.—The impedance of transition metal oxide cathodes is known to increase over the course of long-term cycling. Therefore, for this study, ASI response was measured and compared at BOL in order to isolate the morphological contributions to the impedance and to probe the inherent differences as much as possible. ASI values of the four samples were measured in full-cells using graphite anodes and higher loading cathode electrodes (9 mg cm^{-2}). A summary of the data is shown in Fig. 5. Initially, each cathode underwent an activation up to 4.6 V (vs graphite) followed by a discharge to 2.5 V. The cells were then cycled between 4.4–2.5 V for four cycles. The 1st cycle capacities and efficiencies are shown in Table I for all samples including the Li-metal half-cells discussed above. The relative differences observed within each sample set, cycled against Li or graphite, were relatively small (~5 mAh/g, Table I) where the main contribution can likely be attributed to the expected error when testing hand-made cells, as fully investigated in Ref. 32, Long et al. However, an interesting observation is that the samples fired at the highest temperatures (having the largest primaries) show the largest differences between Li and graphite cells. When comparing the 1st cycle charge curves (vs graphite, added to Supplementary), it is evident that the graphite cells experience clear differences in polarization that are not evident in half-cells, where lower loading electrodes (5 mg cm^{-2}) were used. This result demonstrates that as electrode loadings trend towards practical levels, particle engineering becomes even more critical.

After the formation cycles, the ASI values were collected by an HPPC test during the 7th cycle discharge. The values are shown as a function of SOC in Fig. 5b, where 100% SOC is defined as the charge capacity achieved at 4.4 V just before the start of the HPPC test. As discussed above, increasing the firing temperature led to larger primary particles and lower cyclable capacity. This means the electrodes of Fig. 5 are at slightly different states of overall lithium contents, which was initially the same for all samples before cycling. Therefore, an alternative comparison of ASI as a function of capacity is presented in Fig. 5c, which includes capacity lost during the activation and formation cycles, prior to the HPPC/ASI measurements. The losses from each of the four samples (~55– 60 mAh/g) effectively shifts (represented by arrows) the ASI data to higher capacity values. The SOC, with respect to the theoretical capacity of the cathode (311 mAh/g), at the top of charge prior to the HPPC cycle is shown in Fig. 5c for each of the samples. This allows for a direct comparison of the impedance as a function of Li inventory in the oxides ($Li_xMn_{0.53}Ni_{0.28}Co_{0.19}O_y$).

Returning to a comparison of the ASI data between the samples, it is immediately apparent that the impedance increased systematically across the full SOC as the firing temperature of the sample increased in both Figs. 5b and c. One might reason that this difference is mainly related to the difference in surface areas between the samples. However, a comparison of the impedance at ~ 50% SOC between the endpoint samples (i.e., 925 °C–40 Ω-cm^2 vs 1000 °C–92 Ω-cm^2) confirms that the impedance data cannot simply be normalized by the ~4-fold difference in cathode powder specific surface area (Fig. 2). What's more, one might expect that the LLS_925 °C sample, with its smallest primary particle size and highest specific surface area, might undergo more severe electrolyte interactions and damage during high-voltage activation that would lead to *higher* ASI. However, Chen et al. and Teufl et al. have both shown, as has been similarly found here (see Fig. 4 and supplementary data), that observable surface damage is *minimal* during activation and early cycles, as is probed in the ASI data of Fig. 5. Furthermore, preliminary EIS data collected from each LLS sample in symmetric cells (Figure S16), also suggests that the systematic differences in impedance between the samples is diffusional, and not interfacial, in nature. Finally, the images of Fig. 2 and S6 reveal that the small primary, high surface-area particles, may have an advantage in creating secondary particles with higher internal porosities, allowing faster transport of Li from particles to electrolyte throughout.

It has previously been shown that the ASI response of Li/Mn rich materials above ~3.5 V is dominated by surface effects (i.e., cathode/electrolyte interactions) and that the rising portion of the ASI (Ω_{LSOC}) below ~3.5 V is dominated by local structural changes that occur throughout the particles. These changes (i.e., mechanisms of voltage fade/hysteresis) create disordered sites with Li insertion voltages below ~3.5 V, where the severity of Ω_{LSOC} is correlated to the initial Li/Mn content.[6] Therefore, a qualitative comparison of Ω_{LSOC} from the HPPC data was made by removing the offset in ASI values across the sample set (see Fig. 5d). The results reveal that Ω_{LSOC} also increases *earlier* and more dramatically w/increasing calcination temperature. In effect, the higher Ω_{LSOC} for the cathode samples fired at higher temperature means it is more difficult to insert similar capacities in the low-voltage region for the larger particles with lower surface areas, consistent with the results discussed in Fig. 3. When taken in light of systematic differences in particle morphologies, kinetic properties, and reports from the literature,[3,4,6,14] the data here are in accordance with our previous results showing that surfaces alone cannot explain the differences in Ω_{LSOC} of LMR-NMCs,[6] but also go further in revealing that particle morphologies can play a critical role.

To further decouple the influence of morphology from contributions incurred during activation, the impedance of samples prepared at 925 °C and 1000 °C were probed with and without activation. Each unactivated electrode underwent a 1st cycle between 4.3–2.0 V (vs $Li^{+/0}$) and five cycles between 4.3–2.5 V. Both electrodes delivered similar capacities of 146 mAh/g throughout the 6-cycle test. Activated electrodes underwent a 1st cycle between 4.7–2.0 V (vs $Li^{+/0}$) and five cycles between 4.3–2.5 V with similar results as those shown in Fig. 3.

The ASI values during discharge for both the activated and unactivated samples are compared in Fig. 6, as a function of capacity, which includes the capacity lost during the

activation and formation cycles, as was done in Fig. 5c. It is apparent that for unactivated electrodes (Fig. 6a), the LLS_1000 °C electrode, with larger primary particles (lower effective surface area), experienced higher impedance levels throughout the extent of discharge. When the offset between the samples is removed (Fig. 6b), it is also evident that this sample experienced the onset of impedance rise *earlier* in the discharge than the LLS-925 °C electrode. For unactivated electrodes, the rise in ASI at low SOCs has been linked to the sluggish kinetics of an almost full oxide and occurs with most NMC materials. Here, the effects of particle size/surface area can be observed in the absence of activation. Comparison of activated vs unactivated electrodes reveals several interesting observations (Fig. 6a and c). First, the ASI of the LLS_925 °C electrode at higher SOCs (>3.5 V) decreases overall after activation, in agreement with previous studies when particles having the same morphologies are compared.[4,6] Those studies concluded that a more porous, and perhaps overlithiated, surface phase results from the activation process and creates more facile lithium diffusion. Second, the ASI of the LLS_1000 °C electrode shows much less overall change after activation, implying particle morphology effects, in this case, contribute more to the ASI than the changes that may have occurred during activation. This is an interesting result considering the kinetic effects discussed in Fig. 3 and the possibility of limited oxygen loss near the surface of the larger particles during activation.

Thermal analysis.—The LLS_925 °C, LLS_950 °C, LLS_975 °C, and LLS_1000 °C samples were investigated by DSC measurements to understand the effects of particle size and surface area might have on the thermal stability of the cathode. It is well-established that charged cathodes are much less stable in the presence of electrolyte than after rinsing and drying,[41] attributed to the ability of these solvents to act as reducing agents to accelerate the decomposition of the cathode, and to combustion of the solvents with O_2 released by the cathode.[42] Therefore, thermal studies designed to gauge and compare the stabilities of materials for lithium-ion battery applications should make thermal measurements in the presence of a standard electrolyte. We have conducted our measurements using Gen 2 electrolyte (formulation in Experimental section). For further details about the DSC experiments (e.g., repeatability and baseline subtraction) please see supplementary data.

The theoretical capacity (311 mAh/g for all Li removal) and cumulative irreversible capacity loss during formation cycles was used to estimate Li content, Li_xMO_y, assuming all capacity was the result of Li^+ insertion/extraction only. All samples underwent an activation cycle between 4.6–2.0 V (vs $Li^{+/0}$), followed by three formation cycles between 4.45–2.5 V. On the 5th cycle, each of the samples were charged to the same calculated Li content, approx. $Li_{0.3}MO_y$, as the thermal stability of charged cathodes is known to be dependent on the state of lithiation.[43] Fig. 7a shows the DSC results for each of the charged cathodes. All samples exhibited a consistent, major exothermic peak at ~295 °C. However, each sample exhibited a "pre-peak" that varied in area and onset temperature. Samples prepared with higher firing temperature (with larger primary particles, lower surface area) exhibited the lowest pre-peak onset temperature (280, 275, 250, and 235 °C decomposition onset for LLS_925 °C, LLS_950 °C, LLS_975 °C, and LLS_1000 °C, respectively). Additionally, the samples prepared with higher firing temperature exhibited the largest pre-peak areas (i.e., 4%, 5%, 8%, and 13% of total decomposition heat is in the pre-peak for

925 °C, 950 °C, 975 °C, and 1000 °C, respectively). The total heat released during the exothermic reaction generally decreased as the firing temperature increased (Fig. 7b).

To the best of our knowledge, there are no studies on the effect of surface area and particle size on thermal stability of LMR-NMC cathodes. The trend in total heat released by LLS_925 °C, LLS_950 °C, LLS_975 °C, and LLS_1000 °C are consistent with previous works focused on layered (*R-3m*) oxides, showing a slightly decreasing extent of reaction with decreasing surface area, though the effect was small. However, the onset temperatures for the pre-peaks are opposite the trend expected for surface area and reactivity. As a result, the reaction associated with these pre-peaks is of interest.

It is generally understood that exothermic DSC peaks associated with cathode decomposition are associated with oxygen evolution from charged cathodes accompanied by some degree of phase transition/surface reconstruction (e.g, layered (*R-3m*) → disordered layered (*R-3m*) → spinel (*Fd-3m*) → rock salt (*Fm-3m*).[15,19] Similar phase transitions have also been observed in charged LMR-NMC.[22,24,25] This suggests that the "pre-peaks" observed in Fig. 6 might be related to one of the earlier phase transitions of layered → disordered/spinel. As mentioned above, the preliminary gassing studies of LLS_925 °C and LLS_1000 °C (Figure S8), confirm that samples with higher surface areas do undergo more gas evolution during activation than samples with lower surface area. If a relatively larger fraction of the higher-surface-area cathode (surface/volume) undergoes structural reconstruction during activation, it makes intuitive sense that those "pre-reacted" samples exhibit a delayed onset of further thermal reconstruction/decomposition (i.e., the DSC "pre-peak") compared to lower-surface-area samples that showed less gassing/reconstruction during activation and formation cycles. It should be noted that XRD studies were attempted to confirm that the DSC pre-peaks were associated with a layered → spinel phase transition, but the results were inconclusive.

Conclusions

Integrated, layered–layered–spinel cathode powders were prepared by sintering in air at different temperatures, resulting in particles having similar lithium contents, local and long-range structures, and secondary size distributions but with different primary particle sizes, surface areas, and secondary particle porosities. The following observations were made:

- Electrochemical measurements show that larger primary particles lead to slower kinetics that result in lower reversible capacities at a given rate, as well as higher impedance—of particular importance at low SOCs with respect to LMR-NMCs where unique, local structures influence ASI.

- The sample with the lowest sintering temperature (925 °C) retained the smallest primary particles, highest specific surface area, and uniform pores within the secondary particles that may give more particles direct access to electrolyte, which should contribute to improved rate performance.

- Higher surface area particles may undergo more facile surface changes initially during

activation, leading to more thermally stable surfaces as a result. This suggests that incorporating a spinel phase, especially at the surface of Li/Mn rich particles, may be advantageous as a preemptive measure.

The results presented here emphasize the importance of synthesis and processing in order to achieve optimal performance of cathode oxides, where physical properties (morphologies) can enhance or degrade inherent electrochemical properties, related herein to the bulk, local ordering and associated electrochemical mechanisms unique to LMR-NMCs. In particular, it is shown that optimization of particle designs (primary size, secondary porosity, surface area, surface phases) will be critical to enabling high-performance Li/Mn-rich cathode electrodes. Studies to understand the critical factors in optimizing particle architectures with respect to synthesis and process of Mn-rich cathodes are ongoing.

Acknowledgments

Support from the Office of Vehicle Technologies of the U.S. Department of Energy, particularly from David Howell and Peter Faguy, is gratefully acknowledged. The submitted manuscript has been created by UChicago Argonne, LLC, Operator of Argonne National Laboratory ("Argonne"). Argonne, a U.S. Department of Energy (DOE) Office of Science laboratory, is operated under Contract No. DE-AC02–06CH11357. The U.S. Government retains for itself, and others acting on its behalf, a paid-up, nonexclusive, irrevocable worldwide license in said article to reproduce, prepare derivative works, distribute copies to the public, and perform publicly and display publicly, by or on behalf of the Government. The Department of Energy will provide public access to these results of federally sponsored research in accordance with the DOE Public Access Plan. http://energy.gov/downloads/doe-public-access-plan. This research used resources of the Advanced Photon Source and Center for Nanomaterials, DOE Office of Science User Facilities operated for the DOE Office of Science by Argonne National Laboratory under Contract No. DE-AC02–06CH11357.

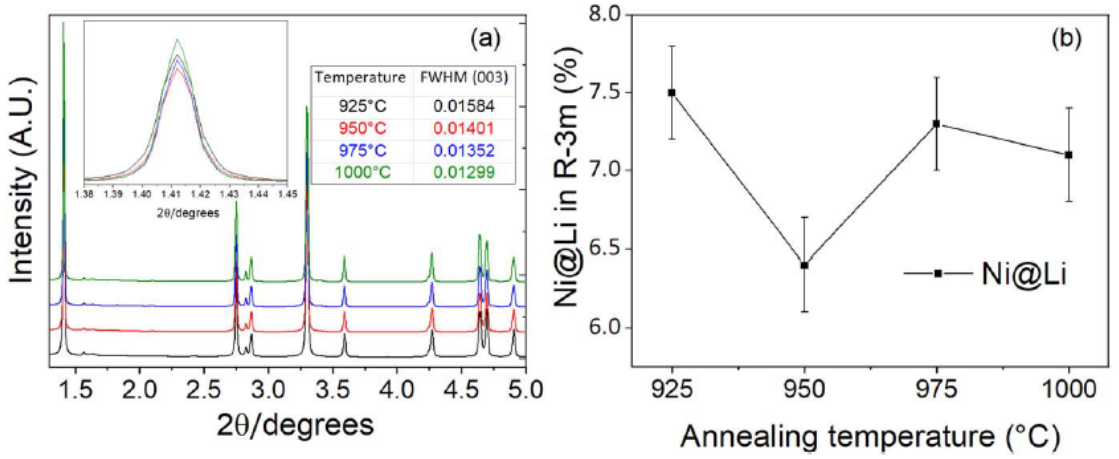

Figure 1. (a) HE-XRD of four LLS powders prepared at 925, 950, 975 and 1000 °C. The inset shows an expanded view of the (003) peak showing the peak broadening of the samples. The table shown in the figure reports the full-width half-maximum of the (003) peak derived from each pattern. (b) Percent Li/Ni mixing for each of the samples determined by Rietveld analysis of neutron powder diffraction data. The standard deviation of Li/Ni mixing for each sample is shown. Details of the analysis are provided in supplementary data.

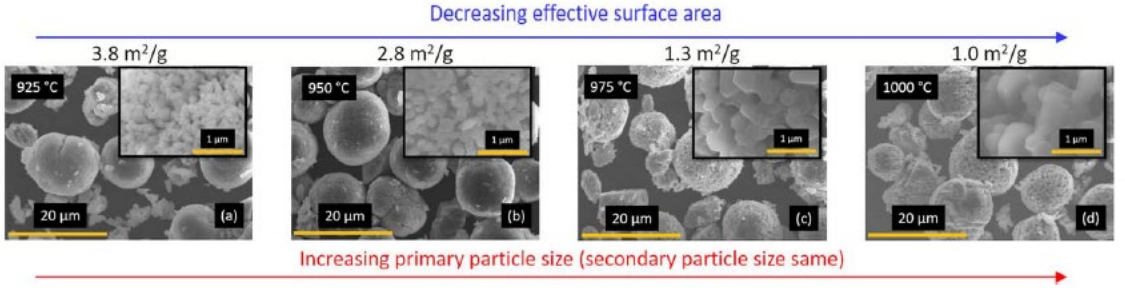

Figure 2. SEM images showing the morphology of the secondary and primary (inset) particles from powders of (a) LLS_925 °C (b) LLS_950 °C (c) LLS_975 °C (d) LLS_1000 °C. The effective surface area for each of the samples, collected using the Brunauer, Emmet and Teller (BET) method, is shown above the images.

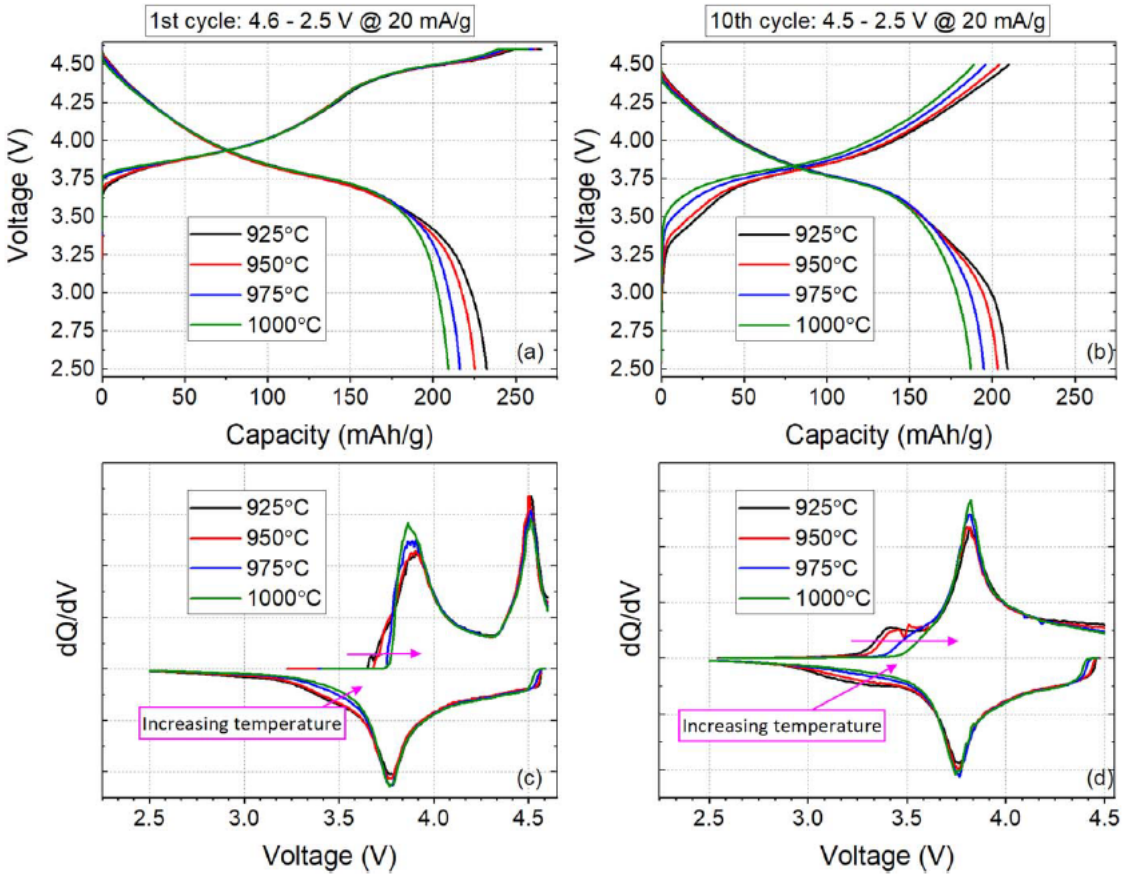

Figure 3. (a)–(b) Voltage profiles and (c)–(d) differential capacity (dQ/dV) of LLS cathodes (vs Li^+/Li^0) prepared at four different temperatures. The data were collected during the (a & c) 1st and (b & d) 10th cycles. The first cycle was between 4.6–2.5 V while the 10th cycle was between 4.5–2.5 V. All cycling was carried out at 20 mA g^{-1} and cells were cycled in a temperature-controlled oven at 30 °C.

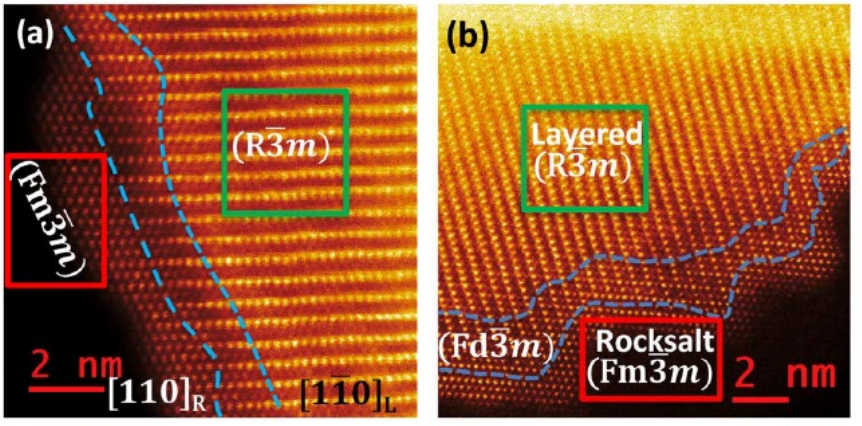

Figure 4. High resolution HAADF-STEM image of selected areas depicting layered-rocksalt intergrown structure on (a) LLS_925 °C and (b) LLS_1000 °C. Both samples underwent four activation cycles before TEM analysis as follows: 1st cycle 4.6–2.0 V, 2nd–4th cycles 4.45–2.5 V.

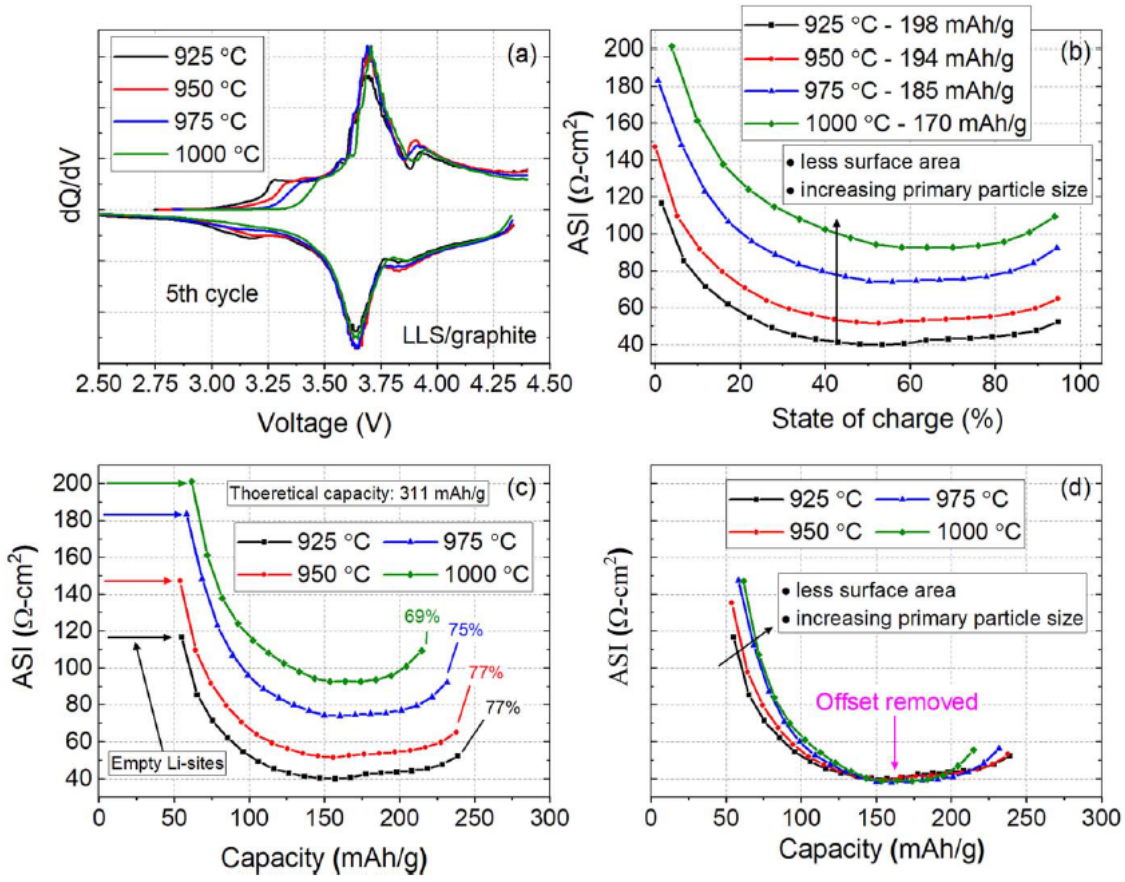

Figure 5. Comparison of full-cell (LLS/graphite) data obtained from the four cathode samples prepared at different temperatures, as labeled in the graphs. (a) dQ/dV curves for the 5th cycle (b) ASI as a function of SOC after formation (collected during 7th cycle discharge). The capacity attained during charging of the 7th cycle is written in the legend. (c) ASI as a function of capacity including a shift (shown by arrows on the *y* axis) representing the amount of capacity lost during the activation and formation cycles preceding the ASI measurements. The percentage values represent the SOC (w/ respect to theoretical capacity) at the top of charge. (d) The ASI data of (c) with the offsets removed.

Table 1. Comparison of 1st cycle cell data from cathode powders cycled in graphite full-cells (9 mg cm^{-2} cathode loading) and Li half-cells (5 mg cm^{-2} cathode loading).

	vs graphite			vs $Li^{+/0}$		
	Charge capacity (mAh/g)	Discharge capacity (mAh/g)	Coulombic efficiency (%)	Charge capacity (mAh/g)	Discharge capacity (mAh/g)	Coulombic efficiency (%)
LLS_925 °C	270	231	86	264	232	88
LLS_950 °C	267	223	84	262	225	86
LLS_975 °C	254	217	85	261	216	83
LLS_1000 °C	245	205	84	257	209	81

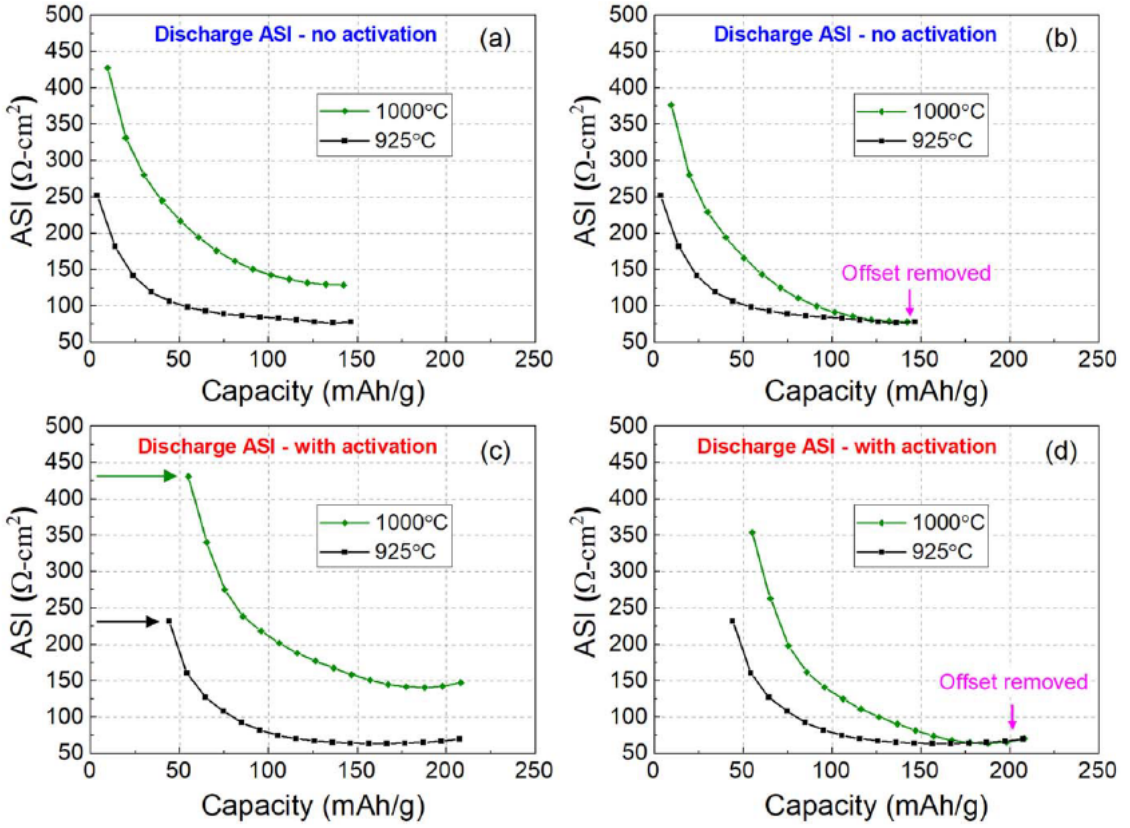

Figure 6. ASI data for LLS_925 °C and LLS_1000 °C as a function of capacity. The capacity values in each of the figures includes a shift representing the amount of capacity lost during the activation and formation cycles (shown by arrows), as was done in figure 5c. All data was collected against Li metal anodes on the 7th cycle discharge. The samples are compared without activation (4.3–2.0 V) in (a) and with the offset between data sets removed in (b); and with activation (4.7–2.0 V) in (c) and with the offset removed in (d). The offset between the samples was removed for qualitative comparison of the impedance rise at low SOCs. All data were collected in a temperature-controlled oven at 30 °C.

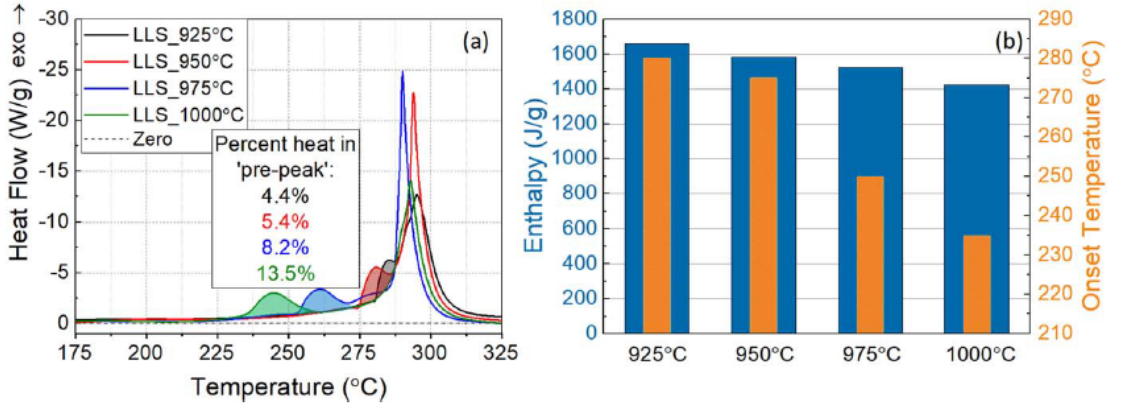

Figure 7. (a) Representative DSC data (baseline-subtracted, mass-normalized) of electrodes made from the cathodes LLS_925 °C, LLS_950 °C, LLS_975 °C, and LLS_1000 °C, all charged to the same calculated Li content, approx. $Li_{0.3}MO_y$, after formation cycles. (b) Averaged heat release and onset temperatures of exothermic reaction between charged cathode and electrolyte during DSC experiment.

References

1. Z. Lu, L. Y. Beaulieu, R. A. Donaberger, C. L. Thomas, and J. R. Dahn, J. Electrochem. Soc., 149, A778 (2002).
2. M. M. Thackeray, C. S. Johnson, J. T. Vaughey, N. Li, and S. A. Hackney, J. Mater. Chem., 15, 2257 (2005).
3. T. Teufl, D. Pritzl, S. Solchenbach, H. A. Gasteiger, and M. A. Mendez, J. Electrochem. Soc., 166, A1275 (2019).
4. T. Teufl, B. Strehle, P. Müller, H. A. Gasteiger, and M. A. Mendez, J. Electrochem. Soc., 165, A2718 (2018).
5. S. R. Gowda, D. W. Dees, A. N. Jansen, and K. G. Gallagher, J. Electrochem. Soc., 162, A1374 (2015).
6. J. Chen, A. Gutierrez, M. T. Saray, R. S. Yassar, M. Balasubramanian, Y. Wang, and J. R. Croy, J. Electrochem. Soc., 168, 080506 (2021).
7. M. Müller, L. Schneider, N. Bohn, J. R. Binder, and W. Bauer, ACS Appl. Energy Mater., 4, 1993 (2021).
8. L. Cheng, B. Zhang, S.-L. Su, L. Ming, Y. Zhao, C.-H. Wang, and X. Ou, J. Alloys Compd., 845, 156202 (2020).
9. J. Zheng, P. Yan, L. Estevez, C. Wang, and J.-G. Zhang, Nano Energy, 49, 538 (2018).
10. J. Liu, H. Chen, J. Xie, Z. Sun, N. Wu, and B. Wu, J. Power Sources, 251, 208 (2014).
11. M. G. Verde, H. Liu, K. J. Carroll, L. Baggetto, G. M. Veith, and Y. S. Meng, ACS Appl. Mater. Inter., 6, 18868 (2014).
12. N. Yabuuchi, K. Kubota, Y. Aoki, and S. Komaba, J. Phys. Chem. C, 120, 875 (2016).
13. Y. Zuo, J. Ma, N. Jiang, and D. Xia, ACS Omega, 3, 11136 (2018).
14. W. Mao, G. Ai, Y. Dai, Y. Fu, X. Song, H. Lopez, and V. Battaglia, J. Electrochem. Soc., 163, A3091 (2016).
15. S. M. Bak, E. Hu, Y. Zhou, X. Yu, S. D. Senanayake, S. J. Cho, K. B. Kim, K. Y. Chung, X. Q. Yang, and K. W. Nam, ACS Appl. Mater. Interfaces, 6, 22594 (2014).
16. I. Belharouak, Y. K. Sun, J. Liu, and K. Amine, J. Power Sources, 123, 247 (2003).
17. H.-J. Noh, S. Youn, C. S. Yoon, and Y.-K. Sun, J. Power Sources, 233, 121 (2013).
18. Y. K. Sun, D. J. Lee, Y. J. Lee, Z. Chen, and S. T. Myung, ACS Appl. Mater. Interfaces, 5, 11434 (2013).
19. I. Belharouak, W. Lu, D. Vissers, and K. Amine, Electrochem. Commun., 8, 329 (2006).
20. D. D. MacNeil, Z. Lu, Z. Chen, and J. R. Dahn, J. Power Sources, 108, 8 (2002).
21. K.-W. Nam, W.-S. Yoon, and X.-Q. Yang, J. Power Sources, 189, 515 (2009).
22. J. Geder, J. H. Song, S. H. Kang, and D. Y. W. Yu, Solid State Ionics, 268, 242 (2014).
23. D. Ouyang, Y. Liu, I. Hamam, J. Wang, and J. Dahn, Journal of Energy Chemistry, 60, 523 (2021).
24. S. Muhammad, S. Lee, H. Kim, J. Yoon, D. Jang, J. Yoon, J.-H. Park, and W.-S. Yoon, J. Power Sources, 285, 156 (2015).
25. C. K. Lin, Y. Piao, Y. Kan, J. Bareno, I. Bloom, Y. Ren, K. Amine, and Z. Chen, ACS Appl. Mater. Interfaces, 6, 12692 (2014).
26. J. R. Croy, D. Kim, M. Balasubramanian, K. Gallagher, S.-H. Kang, and M. M. Thackeray, J. Electrochem. Soc., 159, A781 (2012).
27. B. R. Long, J. R. Croy, J. S. Park, J. Wen, D. J. Miller, and M. M. Thackeray, J.

Electrochem. Soc., 161, A2160 (2014).
28. D. Kim, G. Sandi, J. R. Croy, K. G. Gallagher, S.-H. Kang, E. Lee, M. D. Slater, C. S. Johnson, and M. M. Thackeray, J. Electrochem. Soc., 160, A31 (2012).
29. M. Avdeev and J. R. Hester, J. Appl. Crystallogr., 51, 1597 (2018).
30. A. C. Larson and R. B. Von, Dreele, Los Alamos National Laboratory Report LAUR, 86 (2004).
31. B. H. Toby, J. Appl. Crystallogr., 34, 210 (2001).
32. B. R. Long et al., J. Electrochem. Soc., 163, A2999 (2016).
33. D. P. Abraham, (2020), Cathode Materials for Next Generation Lithium-Ion Batteries: Diagnostics Testing and Evaluation of Low-Cobalt Cathodes, DOE Vehicle Technologies Office Annual Merit Review about Batteries, https://www.energy.gov/eere/vehicles/downloads/cathode-materials-next-generation-lithium-ion-batteries-diagnostic-testing.
34. J. R. Croy, K. G. Gallagher, M. Balasubramanian, Z. Chen, Y. Ren, D. Kim, S.-H. Kang, D. W. Dees, and M. M. Thackeray, J. Phys. Chem. C, 117, 6525 (2013).
35. G. Assat, C. Delacourt, D. A. D. Corte, and J.-M. Tarascon, J. Electrochem. Soc., 163, A2965 (2016).
36. W. E. Gent et al., Nat. Commun., 8, 2091 (2017).
37. G. Assat, D. Foix, C. Delacourt, A. Iadecola, R. Dedryvère, and J.-M. Tarascon, Nat. Commun., 8, 2219 (2017).
38. J. Rana et al., ACS Energy Lett., 5, 634 (2020).
39. Z. W. Lebens-Higgins et al., Materials Horizons, 6, 2112 (2019).
40. N. Li, S. Sallis, J. K. Papp, J. Wei, B. D. McCloskey, W. Yang, and W. Tong, ACS Energy Lett., 4, 2836 (2019).
41. Z. Zhang, D. Fouchard, and J. R. Rea, J. Power Sources, 70, 16 (1998).
42. D. D. MacNeil and J. R. Dahn, J. Electrochem. Soc., 148, A1205 (2001).
43. J. Dahn, E. Fuller, M. Obrovac, and U. Vonsacken, Solid State Ionics, 69, 265 (1994).